

Received November 17, 2020, accepted December 4, 2020, date of publication December 11, 2020, date of current version December 23, 2020.

Digital Object Identifier 10.1109/ACCESS.2020.3044224

# Genetic Algorithm-Based Receiving Resonator Array Design for Wireless Power Transfer

**TAKUYA SASATANI**<sup>1,2</sup>, (Graduate Student Member, IEEE),  
**YOSHIKI NARUSUE**<sup>3</sup>, (Member, IEEE), AND  
**YOSHIHIRO KAWAHARA**<sup>3</sup>, (Member, IEEE)

<sup>1</sup>Graduate School of Information Science and Technology, The University of Tokyo, Tokyo 113-8656, Japan

<sup>2</sup>Japan Society for the Promotion of Science (JSPS), Tokyo 102-0083, Japan

<sup>3</sup>Graduate School of Engineering, The University of Tokyo, Tokyo 113-8656, Japan

Corresponding author: Takuya Sasatani (sasatani@agk.t.u-tokyo.ac.jp)

This work was supported in part by the Grant-in-Aid for JSPS Fellows under Grant JP18J22537, and in part by the Japan Science and Technology Agency (JST), Exploratory Research for Advanced Technology (ERATO) under Grant JPMJER1501.

**ABSTRACT** Deploying 2-D arrays of multiple transmitters is a promising approach for extending wireless power transfer (WPT) to wide surfaces. However, these arrays involve “null zones,” where the transfer efficiency drops significantly. Although this problem can be hypothetically addressed by employing a receiver array and dynamically selecting the appropriate transmitter/receiver pair, designing receiver arrays that achieve high efficiency throughout the surface remains a challenging task. In this study, we propose a genetic algorithm (GA)-based approach to designing receiver arrays free of “null zones”. The main objective is enhancing worst-case scenarios, which in contrast to improving best-case scenarios, reveals significant complexities due to the need for considering numerous possible placements. We overcome this problem by establishing a design flow that leverages the simulated transfer efficiency at numerous positions throughout the surface. Our approach increased the simulated transfer efficiency at the worst position from 3.8% to 42.6%, and we confirmed these results through measurements at the extracted points.

**INDEX TERMS** Genetic algorithm, magnetic resonance coupling, wireless power transfer.

## I. INTRODUCTION

Wireless power transfer (WPT) is being increasingly adopted as a key technology for conveniently powering ubiquitous electronic devices (e.g., mobile phones, laptops, etc.). Various approaches for WPT have been explored, including microwave WPT [1], [2], laser WPT [3], [4], inductive WPT [5], [6], capacitive WPT [7], and 2-D waveguide-based WPT [8], [9]. In particular, WPT via magnetic resonant coupling (WPT-MRC) allows efficient powering under misaligned conditions, which makes it a promising technology for autonomous charging [10]–[17].

A primitive WPT-MRC system consists of a transmitter (TX) resonator that generates an oscillating magnetic field and a receiver (RX) resonator that receives energy via electromagnetic induction. As WPT-MRC is based on the near field, the power transfer efficiency rapidly decreases as the distance between the TX/RX pair increases [5], [18], [19]. Several approaches have been explored to

extend the range, such as TX coils with special wiring patterns [6], [20], [21], 3D cavity-based TXs [22]–[24], and large-scale 2D TX resonator arrays [25]–[30].

In particular, 2-D TX arrays offer advantages such as flexible layout and convenient installation [27], [28]. Typical 2-D TX arrays dynamically activate the TX most strongly coupled to the RX to achieve high efficiency throughout the deployed surface. However, these 2-D TX arrays involve “null zones,” where the retrorse magnetic fields are canceled out and the efficiency drops significantly near the edges of each TX [31], which requires users to avoid these areas when placing devices. These “null zones” may be resolved by packing multiple receivers as an array, which conceptually resembles array antennas used for enhancing the channel diversity in far-field communication systems [32]. However, the design method of these arrays remains an unsolved challenge [33].

While many studies on resonator design have successfully enhanced the efficiency at the “best positions” [34], [35], designing RXs that enhance the “worst position” efficiency is challenging owing to the need for considering the coupling at numerous positions. This challenge becomes more

The associate editor coordinating the review of this manuscript and approving it for publication was Chunsheng Zhu .

complex when multiple TXs/RXs are integrated. Meanwhile, computational methods such as the genetic algorithm (GA) have been used to successfully solve many complex problems in the field of wireless technology, such as antenna design, channel assignment, and system control [36]–[41].

In this study, we propose an approach for designing RX arrays free of “null zones” by leveraging the GA. By leveraging the GA for considering numerous placements on the TX resonator array, the efficiency in the worst case can be improved. We note that preliminary results based on this method were presented in [42]. This study extends the aforementioned study in the following aspects:

- A full description of the proposed approach, including the design considerations of the GA, details of the resonator shape encoding, and a precise description of the studied system.
- Analysis of an additional RX coil array encoding, which provides a better understanding of the proposed approach.

The remaining of this article is organized as follows. Section II describes the studied WPT system and Section III describes the proposed RX resonator array design method. Section IV presents evaluations of the designed RX resonator array through simulations and measurements. Finally, Section VI concludes the paper.

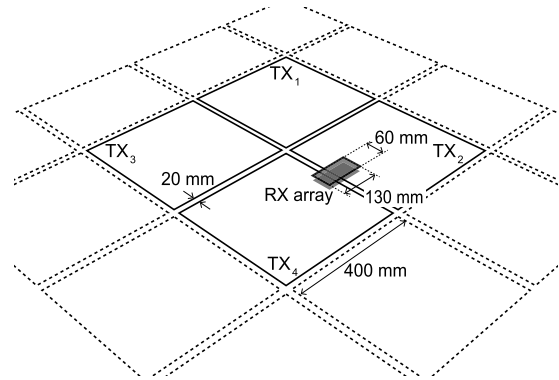
## II. SYSTEM MODEL

A WPT-MRC system with multiple TX and RX resonators is considered in this study. Hereafter, we refer to these TX and RX sets as TX resonator arrays and RX resonator arrays, respectively. The geometry and the equivalent circuit of the considered system are shown in Fig. 1 and Fig. 2, respectively.

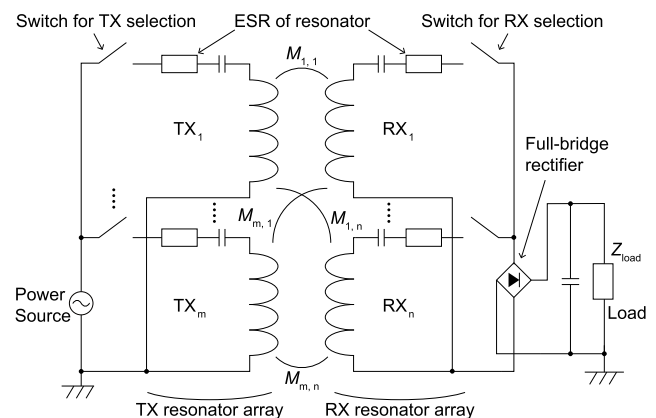
### A. SYSTEM LAYOUT

Fig. 1 shows an overview of the studied system. The TX array was composed of 400 mm × 400 mm loop resonators with a 20-mm gap. The RX array was composed of 2 or 4 loop resonators fitting in a mobile-phone-sized 130 mm × 60 mm rectangular plane. Overlap between the resonators was not allowed to preserve their thinness and compatibility with low-cost manufacturing processes such as printed circuit board (PCB) processes for future deployment. All the resonators were composed of copper wire having a diameter of 1 mm for simplicity. The connected series capacitor tunes the resonant frequency to 6.78 MHz, which is used as an industrial, scientific, and medical (ISM) band. Premising usage scenarios such as a mobile phone (RX) casually placed on a desk (TX), the TX and RX arrays were assumed to face each other with a fixed gap of 10 mm.

We note that while the coil weight is critical in mobile applications, the skin depth of copper in the used frequency bands is ~20 μm, which allows the use of thin, light-weight conductors with minimum loss in efficiency. Moreover, the standards that ride on this frequency band (e.g., AirFuel) often fabricate coils using PCBs instead of rigid wires. As our



**FIGURE 1.** Geometry of the proposed WPT-MRC system, consisting of a TX resonator array and an RX resonator array. For the TX, the outlines indicate the coil pattern, whereas for the RX, the outline of the whole array is shown.



**FIGURE 2.** Equivalent circuit of the studied WPT-MRC system.

approach can be easily applied to PCB processes, multiple coils can be deployed with nearly no addition in weight.

### B. PRINCIPLE OF OPERATION

The equivalent circuit of the studied system is shown in Fig. 2. Only one TX resonator and one RX resonator within the arrays are activated at once. Therefore, when the total numbers of TX and RX resonators in the system are  $m$  and  $n$ , respectively, there will be  $m \times n$  available pairs.

In this selection, the obtainable transfer efficiency for all pairs of RX and TX resonators is evaluated, and the pair with the highest efficiency is solely activated. Both the TX and the RX resonators can be selected by controlling the relays. This procedure requires a communication link to feed the received power back to the TX, and this selection process can be easily introduced as most WPT standards such as AirFuel and Qi have integrated communication protocols (e.g., load-modulation, Bluetooth.) [43], [44]. Note that while the resonators within the array are close to each other, the non-active resonators are left open; hence, no current flows and cross-coupling can be practically ignored.

Using the numbers of TX and RX resonators,  $m$  and  $n$ , and representing the transfer efficiency using the  $i$ -th TX and the

$j$ -th RX as  $\eta_{\text{TX}_i, \text{RX}_j}$ , the transfer efficiency of the WPT-MRC system,  $\eta$ , can be expressed as

$$\eta = \max_{\substack{i=1,2,\dots,m \\ j=1,2,\dots,n}} \eta_{\text{TX}_i, \text{RX}_j}. \quad (1)$$

### C. EQUIVALENT CIRCUIT

In the design process, the transfer efficiency was computed by modeling the TXs and RXs as pairs of inductively coupled LC resonators, as shown in Fig. 3. The design of the RX array is iteratively updated based on this computed transfer efficiency. The circuit parameters  $M$ ,  $R_{\text{TX}}$ ,  $R_{\text{RX}}$  are required for this evaluation, and as a large number of evaluations are necessary to execute the GA, the parameters fixed through this iterative design process ( $R_{\text{TX}}$ ) were obtained using Ansoft HFSS, an FEM-based electromagnetic solver, whereas the parameters that change over the iterations ( $M$ ,  $R_{\text{RX}}$ ) were calculated by following analytical methods that involve a relatively low computational burden. The mutual inductance  $M$  was calculated using the Neumann formula as follows [18]:

$$M = \frac{\mu_0}{4\pi} \oint_{C_1} \oint_{C_2} \frac{ds_1 \cdot ds_2}{d}, \quad (2)$$

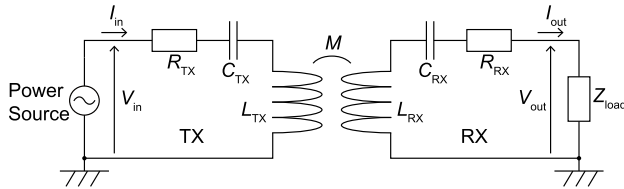


FIGURE 3. Equivalent circuit used for the evaluation of transfer efficiency.

where  $C_1$  and  $C_2$  are the routes of the conductive line of the TXs and RXs, respectively,  $\mu_0$  represents the space permeability, and  $d$  represents the distance between the differential sections  $ds_1$  and  $ds_2$ . The ESR of the RX resonators,  $R_{\text{RX}}$ , was calculated as the product of the wire length and the resistance per unit length considering the skin effect at 6.78 MHz. The capacitors were selected such that they satisfy the following conditions [19]:

$$\omega_0 = 2\pi f_0 = \frac{1}{\sqrt{L_{\text{TX}_i} C_{\text{TX}_i}}} = \frac{1}{\sqrt{L_{\text{RX}_j} C_{\text{RX}_j}}}, \quad (3)$$

where  $L_{\text{TX}_i}$ ,  $C_{\text{TX}_i}$ ,  $L_{\text{RX}_j}$ , and  $C_{\text{RX}_j}$  represent the self-inductance and series capacitance of the  $i$ -th TX resonator and  $j$ -th RX resonator, as shown in Fig. 3. The power source was assumed to be a  $0\Omega$  power source such as a class-D switching amplifier. We defined the transfer efficiency as the proportion of the power consumed by the load to the total power consumption. We assumed that the load impedance tracks the value that maximizes the transfer efficiency, considering prior studies on maximum efficiency point tracking mechanisms [45], [46]. The resulting load impedance  $Z_{\text{load}}$

and transfer efficiency  $\eta_{\text{TX}_i, \text{RX}_j}$  are given as follows [47]:

$$Z_{\text{load}} = \sqrt{\left\{ R_{\text{RX}_j} + \frac{(\omega_0 M_{i,j})^2}{R_{\text{TX}_i}} \right\} R_{\text{RX}_j}}, \quad (4)$$

$$\eta_{\text{TX}_i, \text{RX}_j} = \frac{P_{\text{out}}}{P_{\text{in}}} = \frac{\text{Re}(V_{\text{out}} \cdot \overline{I_{\text{out}}})}{\text{Re}(V_{\text{in}} \cdot \overline{I_{\text{in}}})} = \frac{(\omega_0 M_{i,j})^2}{\left\{ \sqrt{R_{\text{TX}_i} R_{\text{RX}_j}} + \sqrt{R_{\text{TX}_i} R_{\text{RX}_j} + (\omega_0 M_{i,j})^2} \right\}^2}, \quad (5)$$

where  $R_{\text{TX}_i}$  and  $R_{\text{RX}_j}$  represent the ESR of the  $i$ -th TX resonator and the  $j$ -th RX resonator, respectively.

### III. GENETIC ALGORITHM-BASED DESIGN OF RECEIVING RESONATOR ARRAYS

To increase the minimum transfer efficiency of the WPT-MRC system based on a TX resonator array, we present a GA-based RX resonator array design method. This section presents a brief overview of the GA, followed by a description of the encodes and the cost function used in this study. Finally, the GA-based design process is executed and a WPT-MRC system operating at 6.78 MHz is designed.

#### A. GENETIC ALGORITHM

The GA is one form of evolutionary algorithms (EA), which mimics the features of natural selection such as mutation, crossover, and selection [37]. In general, GA is classified into metaheuristics, which are stochastic algorithms known for the capability to deal with various ‘‘hard’’ optimization problems [48], [49]. Metaheuristics typically involve the following operations: (i) selecting the current best solutions and (ii) randomization. The selection operation ensures to hold superior solutions, and the randomization operation prevents the solution from being stuck in local optimums.

GA, which we use in this study, is based on the feedback obtained from the cost function, which is a function of the target parameters in the optimization process. Any requirement can be considered as long as a cost function can represent it. Following Similarly to other metaheuristics, GA adopts two operations that integrate randomness to reach superior solutions rapidly without falling into undesired local optima. One operation is the mutation operation, which adds randomness to individuals, and the other is the crossover operation, which mixes two individuals with a random proportion.

To implement the GA, we need the following two components: (a) an encode representing the individuals as vectors called chromosomes, and (b) a cost function to evaluate the chromosomes. As for the GA framework, we used the GA function available in the MATLAB global optimization toolbox [50]. We presented a detailed description of the implemented GA in Appendix A.

**B. ENCODES OF THE RECEIVING RESONATOR ARRAY**

To execute a GA that designs the geometry of the RX array, we need to encode the coil pattern into a chromosome vector. The elements contained in the chromosomes can be binary, integral, real, or a mixture of the three [39]. As geometry is often expressed by parameters with real numbers such as length or angle (e.g., Cartesian coordinates and polar coordinates), we used vectors of real numbers as chromosomes. The geometries are encoded into the chromosomes by using the length of the arrows shown in encode 1, 2, and 3 in Figs. 4a, 4b, and 4c as parameters. The RX resonators were designed to form a closed loop constructed by polygonal lines. Encode 1, 2, and 3 used 7, 9, and 16 real parameters, respectively, which were all normalized to 1 as described in Appendix III-B. From below, each chromosome is represented by a vector  $(a_1, \dots, a_l) \in \mathbf{R}^l$ , where  $l$  is the dimension of the vector. Minimal exception handling was implemented to prevent the conductive lines from intersecting and to restrict the size of the RX resonator arrays to the required size. The details of each encode are presented in Appendix III-B.

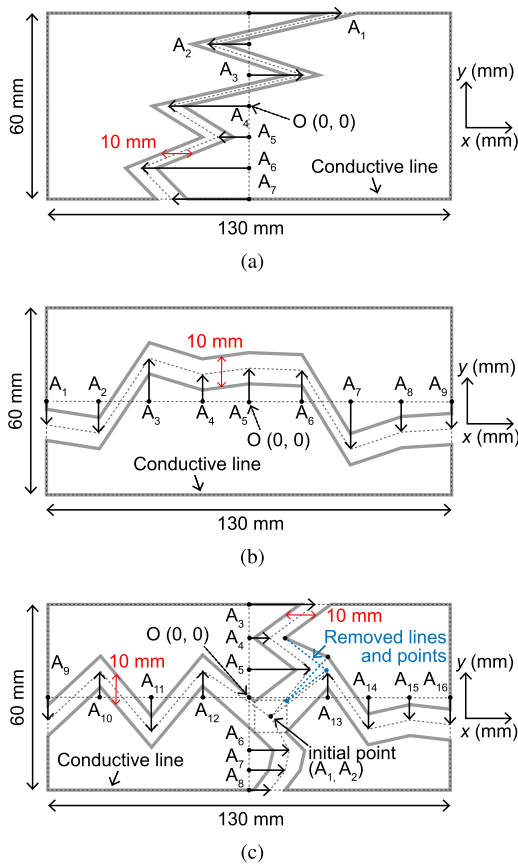
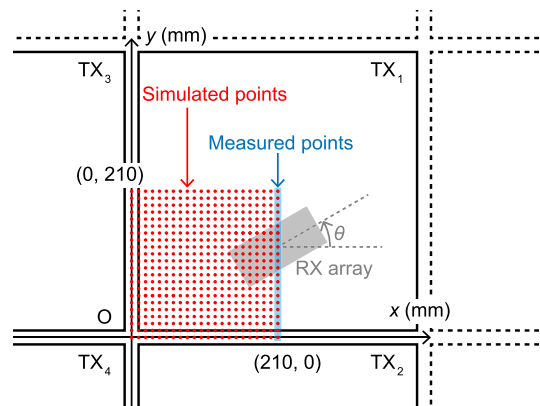


**FIGURE 4.** Encodes of RX resonator arrays used in this study. The gray lines represent the conductive line. The sizes of these arrays were fixed to 130 mm x 60 mm. Note that these shapes are random shapes generated from each encodes to provide an overview of the encodes. (a) Encode 1. (b) Encode 2. (c) Encode 3.

**C. COST FUNCTION: MINIMUM TRANSFER EFFICIENCY**

The GA searches for the chromosome that minimizes or maximizes the cost function. Considering the goal of this study, we selected the minimum transfer efficiency of the WPT-MRC system, (i.e., the efficiency in the “worst case”), as the cost function to be maximized. However, finding the exact value of the minimum transfer efficiency is difficult because of the spatial continuity. Therefore, we defined a spatially discretized version of the minimum transfer efficiency  $\eta_{\min, \Delta d, \Delta \theta}$ , which can be obtained by evaluating the transfer efficiency at discrete points and angles as described below. We defined the lattice points of  $\Delta d$  mm spacing as simulated points. The simulated points for  $\Delta d = 10$  are shown in Fig. 5. We placed the RX array at each of these points and varied the angle of the RX array,  $\theta$ , shown in Fig. 5, from  $0^\circ$  to  $360^\circ$  in steps of  $\Delta \theta^\circ$ . Next, we evaluated  $\eta$  in (1) at each of these points and angles. Note that we activated the pair of TX and RXs that achieves the highest transfer efficiency at each point and angle, as described in Section II. Assuming the 2-D symmetry of the TX array, evaluations at the simulated points shown in Fig. 5 are equivalent to evaluations throughout the surface. When we place the RX array on the simulated points shown in Fig. 5, the TXs excluding TX<sub>1</sub>, TX<sub>2</sub>, TX<sub>3</sub>, and TX<sub>4</sub> are sufficiently far compared to these 4 TXs; therefore, we ignored the transfer efficiencies using the other TXs. We defined the minimum  $\eta$  obtained throughout this operation as  $\eta_{\min, \Delta d, \Delta \theta} \cdot \eta_{\min, \Delta d, \Delta \theta}$  can be expressed using the transfer efficiency  $\eta$  at each point and angle shown in (1) and  $x$ ,  $y$ , and  $\theta$  from Fig. 5 as follows:

$$\eta_{\min, \Delta d, \Delta \theta} = \min_{\substack{x=0, \Delta d, \dots, 210 \\ y=0, \Delta d, \dots, 210 \\ \theta=0, \Delta \theta, \dots, 360}} \eta \quad (6)$$

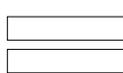
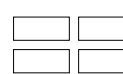


**FIGURE 5.** Simulated and measured points on the TX resonator array. The points show the positions where the centers of the RX resonator arrays were placed for evaluation. Considering the symmetry and periodicity of the TX resonator array, the whole surface can be evaluated by the presented simulated points.

**D. GENETIC ALGORITHM-BASED DESIGN PROCESS**

We executed the GA-based RX array design method using the encodes described in Section III-B and the cost

**TABLE 1. Designed RX resonator arrays and simulated minimum transfer efficiency.**

	(a)	(b)	(c)	(d)	(e)	(f)	(g)
RX Array							
Encode	–	1 (Fig. 4a)		2 (Fig. 4b)		3 (Fig. 4c)	
$\eta_{\min,10,15}$	3.8 %	14.3 %	32.3 %	14.3 %	17.9 %	28.7 %	42.6 %
$(x, y \text{ (mm)}, \theta \text{ (}^\circ\text{)})$	(210, 0, 45)	(110, 0, 0)	(10, 40, 300)	(110, 0, 0)	(190, 10, 285)	(210, 210, 135)	(40, 210, 330)
$\eta_{\min,5,5}$	3.8 %	14.3 %	18.7 %	14.3 %	16.5 %	28.7 %	41.8 %
$(x, y \text{ (mm)}, \theta \text{ (}^\circ\text{)})$	(210, 0, 45)	(110, 0, 0)	(0, 105, 100)	(110, 0, 0)	(10, 195, 190)	(210, 210, 135)	(15, 35, 305)

function  $\eta_{\min,\Delta d,\Delta\theta}$  described in Section III-C; the details are presented in Appendix A. We set the interval parameters  $\Delta d$  and  $\Delta\theta$  to 10 and 15, respectively, to achieve a trade-off between high resolution and quick convergence. Using  $\Delta d = 10$  and  $\Delta\theta = 15$ ,  $\eta_{\min,\Delta d,\Delta\theta}$  requires  $10^5$  calculations of the Neumann formula shown in (2) for evaluating a single RX array, which involves a high computational burden; therefore, it is necessary to keep the number of cost function calculations as small as possible.

The speed of convergence is dependent on the population size and mutation rate. The population size is the number of individuals in a generation and the mutation rate is the proportion of mutation children in a generation. The optimal values of these parameters are strongly dependent on the characteristic of the cost function  $\eta_{\min,\Delta d,\Delta\theta}$ , which is extremely difficult to analyze owing to the complexity and discontinuity of the function. Therefore, we followed the suggestions of prior studies on GA-based antenna design [37]. These studies indicate that a small population improves the performance in early generations and a large population improves the performance in later generations, whereas a low mutation rate results in improvement as a group and a high mutation rate results in improvement in random individuals. Considering this trend, the population size, mutation rate, and number of generations were set to 30, 0.2, and 30, respectively.

This results in approximately  $10^3$  calculations of the cost function  $\eta_{\min,\Delta d,\Delta\theta}$  in the entire design process, which corresponds to approximately  $10^3 \times 10^5 = 10^8$  calculations of the Neumann formula. Here, we note that the aim of the GA used in this study is to find a superior local optimum within a reasonable computation time rather than to find a global optimum. We executed the GA-based design process four times for each encode using a 24-thread parallel calculation on a 2.60 GHz, 24-core virtual machine. The computation time required for each design process was approximately 5 to 10 days depending on the number of RX resonators in the encode. Figs. 6a, 6b, and 6c show the largest  $\eta_{\min,10,15}$  values obtained in each generation of the four trials for each encode. We can observe that encode 3, which has more parameters than the other two encodes, requires more iterations to converge. The designed arrays with the largest  $\eta_{\min,10,15}$  value for each encode are presented in Table 1c, 1e, and 1g. The  $\eta_{\min,10,15}$  values of the simple-shaped RX resonator arrays are

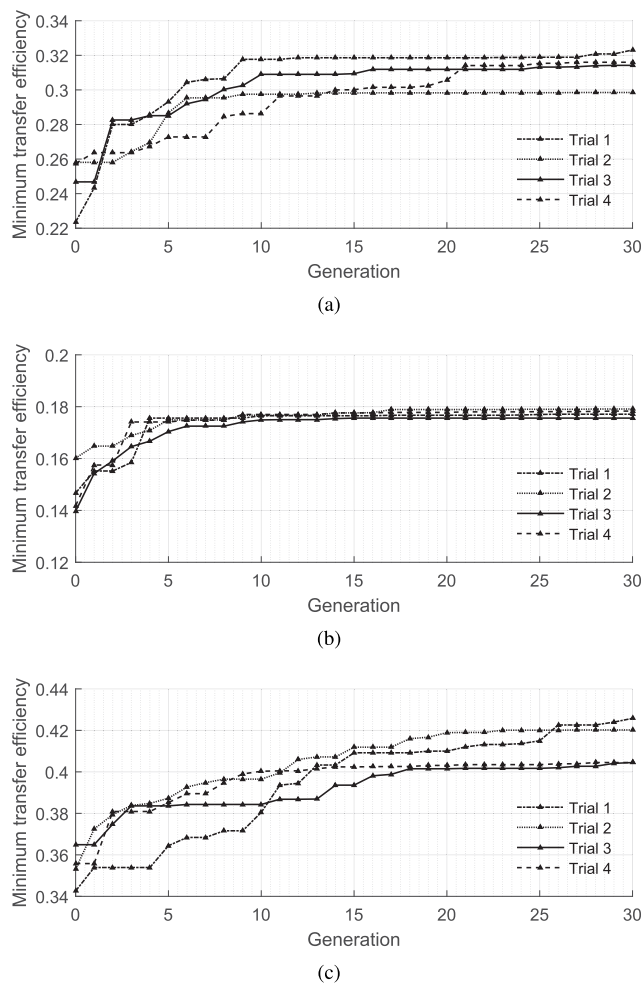


**FIGURE 6. Best simulated minimum transfer efficiency  $\eta_{\min,10,15}$  for each generation. Each line represents a trial. Note that these trials are numbered randomly. (a)Encode 1. (b)Encode 2. (c)Encode 3.**

also presented in Table 1a, 1b, 1d, and 1f to show the baseline. The position and angle of the RX resonator array when it obtained the minimum transfer efficiency are expressed in parentheses below the efficiency value. The results show that  $\eta_{\min,10,15}$  improved to 32.3%, 17.9%, and 42.6% using encode 1, 2, and 3, respectively, whereas a single RX showed a value of 3.8%.

#### IV. SIMULATION AND MEASUREMENT

We additionally conducted evaluations based on simulations with higher spatial resolution and measurements at extracted positions to confirm the simulated results in the previous section.

##### A. SIMULATION WITH HIGHER SPATIAL RESOLUTION

In the design process, we set  $\Delta d$  and  $\Delta\theta$  for  $\eta_{\min,\Delta d,\Delta\theta}$  to 10 and 15, respectively, to achieve a trade-off between accuracy and quick evaluation. Here, we performed a simulation with a higher spatial resolution for a more accurate evaluation; we evaluated  $\eta_{\min,\Delta d,\Delta\theta}$  of each RX resonator array with the resolution parameters set to  $\Delta d = 5$  and  $\Delta\theta = 5$ . Table 1 lists the resulting values of  $\eta_{\min,5,5}$  and it shows that designing an RX resonator array using  $\eta_{\min,10,15}$  as the cost function also improves  $\eta_{\min,5,5}$  in most encodes. However, the RX resonator array designed using encode 1 resulted in a large difference between the values of  $\eta_{\min,10,15}$  and  $\eta_{\min,5,5}$ . The positional dependence of  $\eta$  shown in (1) was investigated to determine the qualitative reason for this difference.

##### B. INSIGHTS FOR EFFICIENCY IMPROVEMENT

To investigate typical trends, we show the  $\eta$  value at each position with  $\theta$  fixed to  $0^\circ$  for a single RX resonator and the RX resonator arrays shown in Table 1a, 1c, 1e, and 1g in Figs. 7a, 7b, 7c, and 7d, respectively.

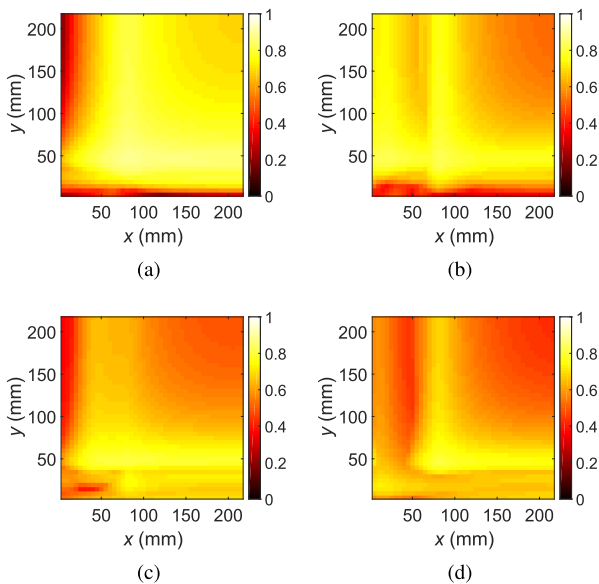


**FIGURE 7.** Simulated transfer efficiency at each position. The  $\theta$  value shown in Fig. 5 is fixed to  $0^\circ$ . The positions correspond to the  $x$ -axis and  $y$ -axis shown in Fig. 5. The scale bar represents the transfer efficiency. (a) Single RX resonator shown in Table 1a. (b) RX resonator array shown in Table 1c. (c) RX resonator array shown in Table 1e. (d) RX resonator array shown in Table 1g.

In general,  $\eta$  dropped at two regions: near the center of the TXs and near the edges of the TXs. Further,  $\eta$  was minimum at the edges of the TX resonators in the single RX resonator

and RX resonator arrays generated using encodes 1 and 2. By contrast,  $\eta$  was minimum at the center of the TX resonators in the RX resonator arrays generated using encode 3. We can see a qualitative trade-off here, *i.e.*, as the number of RX resonators on the array increases, the  $\eta$  at the edges tends to increase, whereas the  $\eta$  at the center tends to decrease. This implies that the encodes that show similar values of  $\eta$  at the centers and edges of the TX resonators are likely to achieve a higher minimum transfer efficiency.

However, in these two regions,  $\eta$  behaves differently when the position of the RX resonator array is slightly changed: (i)  $\eta$  discontinuously changes near the edges because of the intense fluctuation of the magnetic field amplitude and the uncertainty of the activated resonator pair, whereas (ii) the  $\eta$  at the center fluctuates slowly because the resonator pair that can obtain the best transfer efficiency does not change frequently. This means that if the value of  $\eta$  is minimum at the edges, the spatial resolution will severely affect the value of  $\eta_{\min,\Delta d,\Delta\theta}$ , whereas when  $\eta$  takes the minimum value at the center, the spatial resolution will not cause a noticeable change in the value of  $\eta_{\min,\Delta d,\Delta\theta}$ . From these insights, we observed that the criteria of the encode are as follows: (a) the value of  $\eta$  is minimum near the center of the TX resonators and (b) the value of  $\eta$  at the edges and centers of the TX resonators are similar.

We also noticed that the RX array geometry resulted in a highly asymmetric structure. Some may feel this is non-intuitive, considering the symmetrical setup shown in Fig. 1. Therefore, we provide our observation in the following. The resonator pair that obtains the best transfer efficiency should not frequently change near the center of the TXs; therefore, the largest RX coil (which typically is the most strongly coupled) is likely to determine the  $\eta$  at the center. Thereby, we regard it reasonable that the array is asymmetric and one of the RXs (RX<sub>3</sub> for the case of Fig. 9) is large when the above criteria is met.

##### C. MEASUREMENT

We measured the transfer efficiency and the mutual inductance on the points extracted from the simulated points; the objective of this measurement is to confirm the simulated results. The experimental setup is shown in Fig. 8. The measurements were conducted on two series of positions on the TX resonator array: at equally spaced points on a straight line with the angle of the RX resonator array fixed, and at a single point with the RX resonator array rotated at regular angle intervals. These are indicated by the arrows (a) and (b) in Fig. 8, respectively. The series of measurements indicated by arrow (a) in Fig. 8 is also expressed in Fig. 5 as measured points along with the simulated points; in these measurements, the  $\theta$  value shown in Fig. 5 was fixed to  $\theta = 0^\circ$ . As for the measurements indicated by arrow (b) in Fig. 8, the measured point was fixed to  $(x, y) = (210, 0)$  and the angle of the RX resonator array  $\theta$  shown in Fig. 5 was swept from  $0^\circ$  to  $165^\circ$  in steps of  $15^\circ$ . Note that owing to

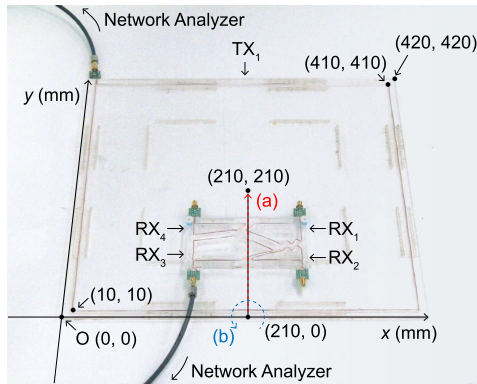


**FIGURE 8.** Experimental setup. Note that measurements considering TX<sub>2</sub> are executed by moving TX<sub>1</sub> symmetrically with respect to the y-axis.

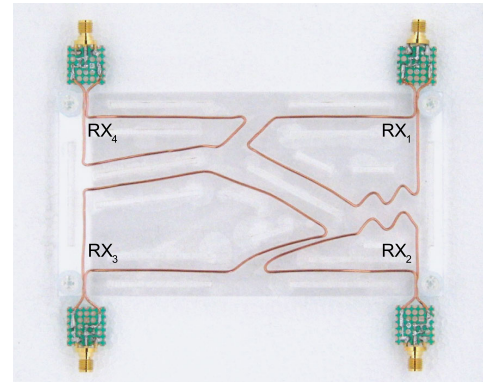


**FIGURE 9.** The RX resonator array presented in Table 1g was fabricated. The detailed geometry of this array is shown in Fig. 10.

the symmetry with respect to the x-axis, this is equivalent to  $\theta$  being swept from 0° to 360° in steps of 15°.

The RX resonator array with the highest  $\eta_{\min,10,15}$  and  $\eta_{\min,5,5}$  values, shown in Table 1g, and a 400 mm × 400 mm TX resonator were fabricated. These coils are composed of 1 mm diameter copper wire, are tuned to 6.78 MHz by soldering series capacitors, and are appended SMA connectors for measurements. The fabricated RX resonator array and the detailed geometry of the array are shown in Fig. 9 and Fig. 10, respectively.

For the measurements of transfer efficiency and mutual inductance, the S-parameters at 6.78 MHz for each position and TX/RX pair were measured using a network analyzer. The transfer efficiency, defined as the proportion of power consumed by the load to the total power consumption, was calculated from these S-parameters by assuming that the load impedance is optimum [45]. This corresponds to the efficiency when the load impedance calculated by (4) is connected; this assumption is known to be promising through prior work. The mutual inductance was calculated using the measured S-parameter; the equivalent circuit is shown in Fig. 2. When the RX resonator array was positioned on the measured points, the simulated transfer efficiencies using TX<sub>3</sub> and TX<sub>4</sub> were low; therefore, the measurements were conducted for only those pairs that included TX<sub>1</sub> and TX<sub>2</sub>. The simulated and measured transfer efficiencies are shown in Fig. 11 and Fig. 12, respectively. Fig. 11 shows the series of evaluation results for arrow (a) shown in Fig. 8. Fig. 12 shows the series of evaluation results for arrow (b) shown in Fig. 8. The simulated and measured mutual inductances are shown in Fig. 13 and Fig. 14, respectively. Fig. 13 shows the series of evaluation results for arrow (a) shown in Fig. 8. Fig. 14 shows the series of evaluation results for arrow (b) shown in Fig. 8. The measured and calculated ESR of the resonators are listed in Table 2. Note that the measured ESR includes the ESR of the series capacitors, and parasitic losses from various non-ideal components (e.g., copper loss of soldering, resistor of connectors, etc.). For the transfer efficiency, although the measured value is lower than the simulated value, the trends correspond well considering the ESR difference.

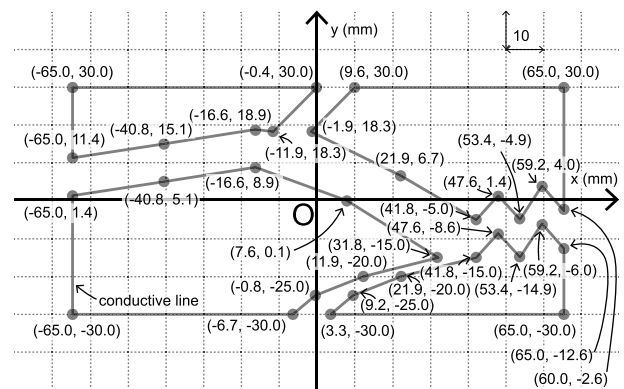


**FIGURE 10.** Detailed geometry of the RX resonator array in Fig.9 and Table 1g. The built-in exception handling mentioned in Section III-B was activated to prevent overlap of the conductive lines. Therefore, the configuration does not strictly match encode 3 shown in Fig. 4c.

**TABLE 2.** ESR of the resonators.

Resonator	TX	RX <sub>1</sub>	RX <sub>2</sub>	RX <sub>3</sub>	RX <sub>4</sub>
Calculated ( $\Omega$ )	0.410	0.042	0.035	0.051	0.034
Measured ( $\Omega$ )	0.517	0.070	0.060	0.091	0.064

Furthermore, the measured mutual inductance and the simulated mutual inductance are in good agreement.

## V. LIMITATIONS AND FUTURE WORK

This section points out two limitations of this study and the relevant directions for future work. First, we limited the scope of this study to “selecting” a single RX element out of the RX array because (i) the system operation procedure becomes simple, and (ii) the optimum load impedance only deviates on the real axis (See (4)). We regard (ii) as a benefit because real impedance can be adjusted with simple hardware (e.g., switching voltage regulator [46]). Meanwhile, an interesting direction to explore is “combining” multiple RX inputs instead of “selecting” a single RX. This approach can ideally achieve higher efficiency; however, we will leave it for future work because such systems will introduce the

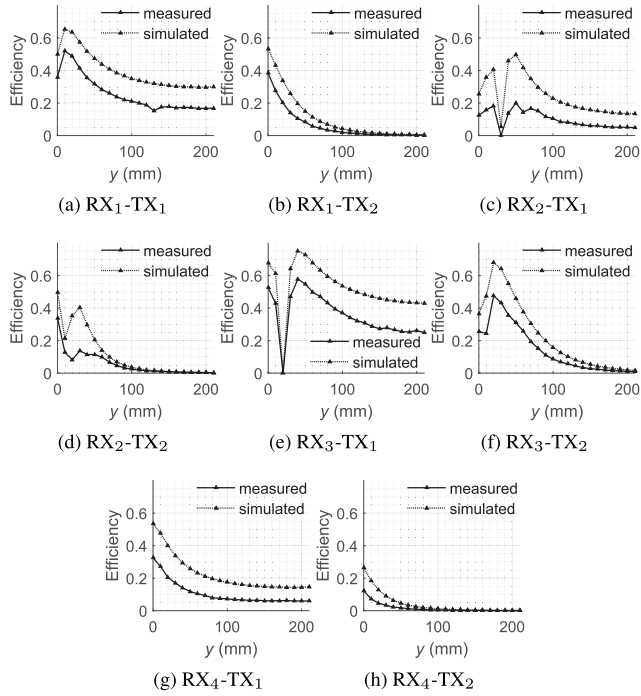


**FIGURE 11.** Transfer efficiency between each pair of TX and RX resonators when using the RX array shown in Fig. 9; the  $y$ -coordinate of the RX array position was varied in these plots. The evaluated points are indicated in Fig. 5; the angle of the RX resonator array,  $\theta$ , also shown in Fig. 5, was fixed to  $\theta = 0^\circ$ .

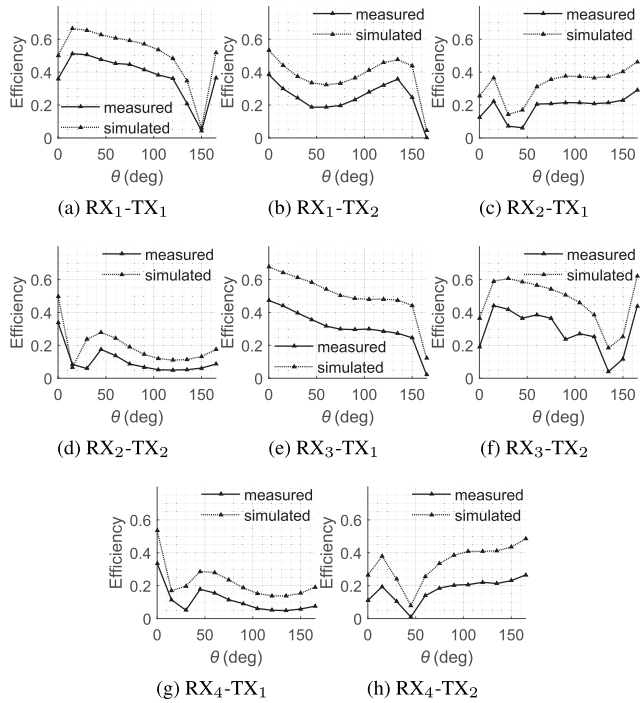


**FIGURE 12.** Transfer efficiency between each pair of TX and RX resonators when using the RX array shown in Fig. 9; the angle of the RX resonator array,  $\theta$ , shown in Fig. 5, was varied in these plots. The position of the RX resonator array was fixed to  $(x, y) = (210, 0)$ .

following challenges: (i) combining power in the proper proportion requires a complex system configuration that

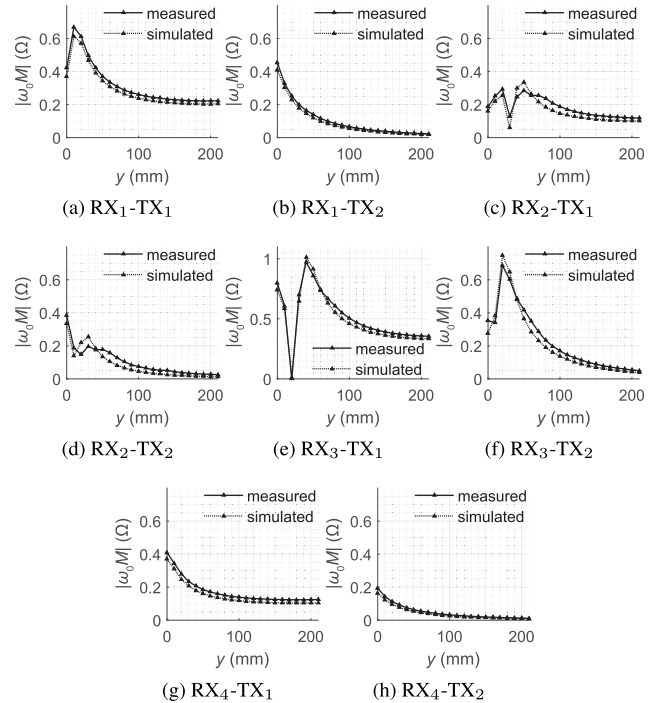


**FIGURE 13.**  $|\omega_0 M|$  value between each pair of TX and RX resonators when using the RX array shown in Fig. 9; the  $y$ -coordinate of the RX array position was varied in these plots.  $\omega_0$  and  $M$  represent the operating angular frequency and mutual inductance, respectively. The evaluated points are indicated in Fig. 5; the angle of the RX resonator array,  $\theta$ , also shown in Fig. 5, was fixed to  $\theta = 0^\circ$ .

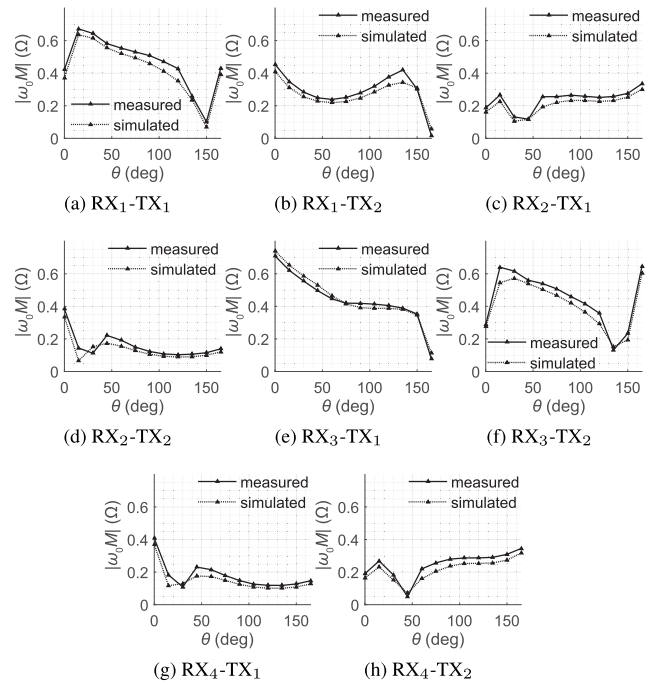


**FIGURE 14.**  $|\omega_0 M|$  value between each pair of TX and RX resonators when using the RX array shown in Fig. 9; the angle of the RX resonator array,  $\theta$ , shown in Fig. 5, was varied in these plots.  $\omega_0$  and  $M$  represent the operating angular frequency and mutual inductance, respectively. The position of the RX resonator array was fixed to  $(x, y) = (210, 0)$ .

introduces additional losses, and (ii) cross-coupling effect requires sophisticated hardware for compensation [51], [52].

Another limitation of this study we raise is that we empirically determined the GA's parameters based on previous work [37]. For the problem we dealt with, the design process converged within a reasonable computation time; therefore, we consider that this approach was sufficient. However, if we suppose significantly complex situations, we may need to optimize further the GA's parameters for convergence within practical computation time (*e.g.*, designing 3-D charging systems with six degrees of freedom (6DoF) [53], coil design considering the interference of metallic bodies [54]). As this topic is highly dependent on the considered situation (*i.e.*, cost function and chromosomes), and there is no established method for evaluating GA performance in general setups [37], we leave this exploration for future work.

## VI. CONCLUSION

We proposed a GA-based RX array design method to overcome the challenge in designing RXs based on the "worst case" efficiency throughout the surface. Through this advancement, significant drops in the transfer efficiency can be prevented across the TX resonator array. In addition, we investigated the conditions required for the encodes to achieve high efficiency in the worst case. By employing the RX resonator array designed using the proposed method, the computed minimum transfer efficiency improved to 42.6%, whereas a single RX resonator array showed a value of 3.8%. Finally, the designed RX resonator array was fabricated, and the computed results were confirmed by the measured results at the extracted positions.

## APPENDIX A

### DETAILS OF THE GENETIC ALGORITHM

#### A. ENCODES OF THE RX ARRAY GEOMETRY

##### 1) ENCODE 1

Encode 1 (Fig. 4a) represents the shape of two RX resonators using seven real parameters  $a_1, \dots, a_7$ . As shown in Fig. 4a, the conductive lines on the short edge of the array were fixed to the edges and thus placed on  $x = \pm 65$  mm. The polygonal line boundary that vertically divides the geometry of the RX resonator array was defined by the arrows  $A_i$  ( $i = 1, \dots, 7$ ) shown in Fig. 4a. From below, the coordinates of the end point of arrow  $A_i$  are represented as  $(x_i, y_i)$ . The polygonal line points for the two RX resonators were placed at  $(x_i \pm 5, y_i)$ . The start points of these arrows  $(0, y_i)$  were placed on the  $y$ -axis, vertically dividing the whole RX resonator array at equal intervals. The value of  $x_i$  that represents the length of the arrow  $A_i$  was defined as

$$x_i = x_{\text{low}} + (x_{\text{high}} - x_{\text{low}}) \cdot a_i, \quad (7)$$

where  $a_i$  is the  $i$ -th element of the chromosome and takes a value between 0 and 1 as mentioned above. Further,  $x_{\text{low}}$  and  $x_{\text{high}}$  represent the lower limit and upper limit of  $x_i$ , respectively, and they were set to  $-55$  mm and  $+55$  mm, respectively, to prevent the intersection with the conductive line placed on  $x = \pm 65$  mm. By connecting the

polygonal line points defined in this process as shown in Fig. 4a, the geometry of two RX resonators is decoded.

##### 2) ENCODE 2

Encode 2 (Fig. 4b) represents the shape of two RX resonators using nine real parameters  $a_1, \dots, a_9$ . As shown in Fig. 4b, the conductive lines on the long edge of the array were fixed to the edges and therefore placed on  $y = \pm 30$  mm. The polygonal line boundary that horizontally divides the geometry of the RX resonator array was defined by the arrows  $A_i$  ( $i = 1, \dots, 9$ ) shown in Fig. 4b. From below, the coordinates of the end point of arrow  $A_i$  are represented as  $(x_i, y_i)$ . The polygonal line points for the two RX resonators were placed at  $(x_i, y_i \pm 5)$ . The start points of these arrows  $(x_i, 0)$  were placed on the  $x$ -axis, horizontally dividing the whole RX resonator array at equal intervals. The value of  $y_i$  was defined as

$$y_i = y_{\text{low}} + (y_{\text{high}} - y_{\text{low}}) \cdot a_i, \quad (8)$$

where  $a_i$  is the  $i$ -th element of the chromosome and takes a value between 0 and 1 as mentioned above. Further,  $y_{\text{low}}$  and  $y_{\text{high}}$  represent the lower limit and upper limit of  $y_i$ , and they were set to  $-20$  mm and  $+20$  mm, respectively, to prevent intersection with the conductive line placed on  $y = \pm 30$  mm. Finally, by connecting the polygonal line points defined in this process as shown in Fig. 4b, the geometry of two RX resonators is decoded.

##### 3) ENCODE 3

Encode 3 (Fig. 4c) represents the shape of 4 RX resonators using 16 real parameters  $a_1, \dots, a_{16}$ . As shown in Fig. 4c, one polygonal line point for each conductive loop was fixed to the corner of the whole RX resonator array. The remaining polygonal line points are decoded from the elements of the chromosome as follows. First, based on the first two elements  $a_1, a_2$ , the initial point  $(x, y) = (A_1, A_2)$  shown in Fig. 4c was determined. Elements  $a_1$  and  $a_2$  are substituted into (7) and (8) to obtain  $A_1$  and  $A_2$ , respectively. The  $x_{\text{low}}, x_{\text{high}}, y_{\text{low}}$ , and  $y_{\text{high}}$  values were set to  $-55, +55, -20$ , and  $+20$ , respectively. The four points  $(A_1 \pm 5, A_2 \pm 5)$  were set as polygonal line points for the four resonators as shown in Fig. 4c. The arrows  $A_3, \dots, A_8$  define the polygonal line that vertically splits the RX resonator and the arrows  $A_9, \dots, A_{16}$  define the polygonal line that horizontally splits the RX resonator. The arrows  $A_3, \dots, A_8$  are parallel to the  $x$ -axis, and the arrows  $A_9, \dots, A_{16}$  are parallel to the  $y$ -axis. From below, the coordinates of the end point of arrow  $A_i$  are represented as  $(x_i, y_i)$ . The values  $y_i$  ( $i = 3, \dots, 8$ ) and  $x_i$  ( $i = 9, \dots, 16$ ), which represent the start points of these arrows, are determined as follows. First,  $y_3, y_8, x_9$ , and  $x_{16}$  were set to  $+30, -30, -65$ , and  $+65$ , respectively, as shown in Fig. 4c. Then,  $y_i$  ( $i = 4, 5$ ) were set such that the distance from  $A_2 + 5$  to  $+30$  was equally divided into three segments and  $y_i$  ( $i = 6, 7$ ) were set such that the distance from  $A_2 - 5$  to  $-30$  is equally divided into three segments. Similarly,  $x_i$  ( $i = 10, 11, 12$ ) were set such that the distance

from  $A_1 - 5$  to  $-65$  is equally divided into four segments and  $x_i$  ( $i = 13, 14, 15$ ) were set such that the distance from  $A_1 + 5$  to  $+65$  is equally divided into four segments. Next,  $x_i$  ( $i = 3, \dots, 8$ ) and  $y_i$  ( $i = 9, \dots, 16$ ), which represent the length of the arrows, were determined.  $x_i$  ( $i = 3, \dots, 8$ ) was obtained by substituting  $a_i$  ( $i = 3, \dots, 8$ ) into (7) and  $y_i$  ( $i = 9, \dots, 16$ ) was obtained by substituting  $a_i$  ( $i = 9, \dots, 16$ ) into (8). Here, for  $x_i$  ( $i = 3, \dots, 8$ ), the  $x_{low}$  and  $x_{high}$  values were set to  $-55$  mm and  $+55$  mm, respectively, to prevent intersection with the conductive line placed on  $x = \pm 65$  mm. Meanwhile, for  $y_i$  ( $i = 9, \dots, 16$ ), the  $y_{low}$  and  $y_{high}$  values were adjusted depending on the length of the arrows  $A_4, \dots, A_7$  to reduce the probability of intersection of the conductive lines. The adjusting process for  $y_{low}$  was conducted as follows. Note that the following process was conducted for each arrow  $A_i$  ( $i = 9, \dots, 16$ ); the process ends as soon as a value is set in  $y_{low}$ .

- If  $A_6$  intersects with  $x = x_i$ ,  $y_{low}$  is set to  $y_6 + 10$ .
- If  $A_7$  intersects with  $x = x_i$ ,  $y_{low}$  is set to  $y_7 + 10$ .
- $y_{low}$  is set to  $-20$ .

Similar to  $y_{low}$ , the adjusting process for  $y_{high}$  was conducted as follows. Note that the following process was conducted for each arrow  $A_i$  ( $i = 9, \dots, 16$ ), and the process ends as soon as a value is set in  $y_{high}$ .

- If  $A_5$  intersects with  $x = x_i$ ,  $y_{high}$  is set to  $y_5 - 10$ .
- If  $A_4$  intersects with  $x = x_i$ ,  $y_{high}$  is set to  $y_4 - 10$ .
- $y_{high}$  is set to  $+20$ .

From above, the initial point  $(x, y) = (A_1, A_2)$  and the 14 arrows  $A_3, \dots, A_{16}$  shown in Fig. 4c are determined. The polygonal line points are placed on  $(x_i \pm 5, y_i)$  for  $i = 3, \dots, 8$  and  $(x_i, y_i \pm 5)$  for  $i = 9, \dots, 16$  as shown in Fig. 4c. Finally, by connecting the polygonal line points defined in this process as shown in Fig. 4c, the geometry of four RX resonators are decoded. When intersections of conductive lines occur owing to the twist of the loop as shown in Fig. 4c, the polygonal line indicates that the cause the intersection was removed. The points removed in this manner are indicated in Fig. 4c as removed lines and points. The rule here works as follows: within the polygonal line points that form multiple loops, keep the polygonal line points included in the loop containing the corner of the RX resonator array and remove the other points. After these points were removed, the kept points were connected to form a single conductive loop.

## B. FORMATION OF THE POPULATION

The GA consists of the six operations listed below:

- 1) Formation of the initial population.
- 2) Evaluation of each individual in the current population using the cost function.
- 3) Check if the exit condition is satisfied.
- 4) Selection of the  $N_{elite}$  elite children.
- 5) Formation of the  $N_{mutate}$  mutation children.
- 6) Formation of the  $N_{crossover}$  crossover children.

Note that  $N_{elite}$ ,  $N_{mutate}$ , and  $N_{crossover}$  represent the number of elite, mutation, and crossover children, respectively. Representing the total number of chromosomes in each generation

as  $N_{total}$ , these integers maintain the following relationship:

$$N_{total} = N_{elite} + N_{mutate} + N_{crossover} \quad (9)$$

Operation 1 is executed only in the first instance of the entire process, and operations 2 to 6 are executed repetitively until the exit condition is satisfied in operation 3. In this study, the exit condition was defined by the number of iterations executed. This section presents the operations used to form the populations of chromosomes, which correspond to operations 1, 4, 5, and 6 in the list.

In operation 1, the  $N_{total}$  individuals were generated using uniform random numbers that take a real value between 0 and 1. Operations 4 to 6 create the  $(k+1)$ -th generation of chromosomes based on the evaluation results of the  $k$ -th generation obtained from operation 2. First, through operation 2, the  $N_{elite}$  chromosomes that show the highest values of the cost functions in the  $k$ -th generation are guaranteed to be included in the  $(k+1)$ -th generation. To execute operations 5 and 6, it is necessary to define three methods: a method for selecting parent chromosomes, a method for generating one mutation child chromosome from one parent chromosome, and a method for generating one crossover child chromosome from two parent chromosomes.

### 1) SELECTION OPERATION

In the selection of the parent chromosomes, it is important to have a high probability of selecting chromosomes that show superior performance to reach the local optima rapidly. Furthermore, it is necessary to have a possibility for selecting random chromosomes to avoid falling into a single local optimum. Therefore, many GAs adopt a selection method based on the probability of selection, which is defined to have a positive correlation with the evaluated values of the cost function. This study adopts stochastic universal sampling based on the rank of individuals as the selection method, in which the probability of the selection of an individual with a rank  $R$  is scaled to  $1/\sqrt{R}$  [50], [55].

### 2) MUTATION OPERATION

The mutation operation is usually an operation that changes some of the elements within the chromosomes to different values. In this study, the mutation operation was executed as follows. The number of mutated children in one generation and the length of the chromosome (*i.e.*, the number of elements included in a chromosome) are represented as  $N_{mutate}$  and  $l$ , respectively.

- Select  $N_{mutate}$  chromosomes from the parent generation based on the selection method described in Section A-B1.
- For each element in the  $N_{mutate}$  vectors, replace the element with a uniform random number between 0 and 1 with a probability of  $p_1$ . Here,  $p_1$  is a parameter that represents the probability of mutation; it was set to 20% in this study. Note that this operation will be executed against  $N_{mutate} \times l$  elements.

This process results in  $N_{mutate}$  mutation children.

### 3) CROSSOVER OPERATION

The crossover operation is an operation that combines two chromosomes in the  $k$ -th generation to form one crossover chromosome in the  $(k + 1)$ -th generation. In this study, the crossover operation was executed as follows [50], [56]. The number of crossover children in one generation is represented as  $N_{\text{crossover}}$ .

- Select  $N_{\text{crossover}} \times 2$  chromosomes from the parent generation based on the selection method described in Section A-B1.
- Using the  $N_{\text{crossover}} \times 2$  chromosomes,  $N_{\text{crossover}}$  pairs of chromosomes are formed randomly.
- Representing the pair from the parent generation as  $\mathbf{x}_{\text{parent1}}$  and  $\mathbf{x}_{\text{parent2}}$ , the child chromosome  $\mathbf{x}_{\text{child}}$  is calculated as follows.

$$\mathbf{x}_{\text{child}} = p \cdot \mathbf{x}_{\text{parent1}} + (1 - p) \cdot \mathbf{x}_{\text{parent2}}, \quad (10)$$

where  $p$  is a uniform random number with a range of  $0 < p < 1$ . This step is executed for every pair of parent chromosomes.

This operation forms  $N_{\text{crossover}}$  crossover children.

### REFERENCES

- [1] W. C. Brown, "The history of power transmission by radio waves," *IEEE Trans. Microw. Theory Techn.*, vol. 32, no. 9, pp. 1230–1242, Sep. 1984.
- [2] N. Shinohara, "Power without wires," *IEEE Microw. Mag.*, vol. 12, no. 7, pp. S64–S73, Dec. 2011.
- [3] K. Jin and W. Zhou, "Wireless laser power transmission: A review of recent progress," *IEEE Trans. Power Electron.*, vol. 34, no. 4, pp. 3842–3859, Apr. 2019.
- [4] V. Iyer, E. Bayati, R. Nandakumar, A. Majumdar, and S. Gollakota, "Charging a smartphone across a room using lasers," *Proc. ACM Interact. Mobile Wearable Ubiquitous Technol.*, vol. 1, no. 4, pp. 143:1–143:21, Jan. 2018.
- [5] S. Y. R. Hui, W. Zhong, and C. K. Lee, "A critical review of recent progress in mid-range wireless power transfer," *IEEE Trans. Power Electron.*, vol. 29, no. 9, pp. 4500–4511, Sep. 2014.
- [6] E. Waffenschmidt, "Free positioning for inductive wireless power system," in *Proc. IEEE Energy Convers. Congr. Expo.*, Phoenix, AZ, USA, Sep. 2011, pp. 3480–3487.
- [7] M. Kline, I. Izyumin, B. Boser, and S. Sanders, "Capacitive power transfer for contactless charging," in *Proc. Twenty-Sixth Annu. IEEE Appl. Power Electron. Conf. Expo. (APEC)*, Mar. 2011, pp. 1398–1404.
- [8] A. Noda and H. Shinoda, "Selective wireless power transmission through high- $Q$  flat waveguide-ring resonator on 2-D waveguide sheet," *IEEE Trans. Microw. Theory Techn.*, vol. 59, no. 8, pp. 2158–2167, Aug. 2011.
- [9] X. Tian, P. M. Lee, Y. J. Tan, T. L. Y. Wu, H. Yao, M. Zhang, Z. Li, K. A. Ng, B. C. K. Tee, and J. S. Ho, "Wireless body sensor networks based on metamaterial textiles," *Nature Electron.*, vol. 2, no. 6, pp. 243–251, Jun. 2019.
- [10] A. Kurs, A. Karalis, R. Moffatt, J. D. Joannopoulos, P. Fisher, and M. Soljacic, "Wireless power transfer via strongly coupled magnetic resonances," *Science*, vol. 317, no. 5834, pp. 83–86, Jul. 2007.
- [11] P. S. Riehl, A. Satyamoorthy, H. Akram, Y.-C. Yen, J.-C. Yang, B. Juan, C.-M. Lee, F.-C. Lin, V. Muratov, W. Plumb, and P. F. Tustin, "Wireless power systems for mobile devices supporting inductive and resonant operating modes," *IEEE Trans. Microw. Theory Techn.*, vol. 63, no. 3, pp. 780–790, Mar. 2015.
- [12] L. L. Pon, C. Y. Leow, S. K. A. Rahim, A. A. Eteng, and M. R. Kamarudin, "Printed spiral resonator for displacement-tolerant near-field wireless energy transfer," *IEEE Access*, vol. 7, pp. 10037–10044, Jan. 2019.
- [13] J. Kuang, B. Luo, Y. Zhang, Y. Hu, and Y. Wu, "Load-isolation wireless power transfer with K-inverter for multiple-receiver applications," *IEEE Access*, vol. 6, pp. 31996–32004, Apr. 2018.
- [14] S. Ding, W. Niu, and W. Gu, "Lateral misalignment tolerant wireless power transfer with a tumbler mechanism," *IEEE Access*, vol. 7, pp. 125091–125100, Jan. 2019.
- [15] S. Assaworarith, X. Yu, and S. Fan, "Robust wireless power transfer using a nonlinear parity-time-symmetric circuit," *Nature*, vol. 546, no. 7658, pp. 387–390, Jun. 2017.
- [16] L. Gu, G. Zulauf, A. Stein, P. A. Kyaw, T. Chen, and J. M. R. Davila, "6.78-MHz wireless power transfer with self-resonant coils at 95% DC-DC efficiency," *IEEE Trans. Power Electron.*, vol. 36, no. 3, pp. 2456–2460, Mar. 2021.
- [17] J. Choi, J. Xu, R. Makhoul, and J. M. R. Davila, "Implementing an impedance compression network to compensate for misalignments in a wireless power transfer system," *IEEE Trans. Power Electron.*, vol. 34, no. 5, pp. 4173–4184, May 2019.
- [18] T. Imura and Y. Hori, "Maximizing air gap and efficiency of magnetic resonant coupling for wireless power transfer using equivalent circuit and neumann formula," *IEEE Trans. Ind. Electron.*, vol. 58, no. 10, pp. 4746–4752, Oct. 2011.
- [19] A. P. Sample, D. A. Meyer, and J. R. Smith, "Analysis, experimental results, and range adaptation of magnetically coupled resonators for wireless power transfer," *IEEE Trans. Ind. Electron.*, vol. 58, no. 2, pp. 544–554, Feb. 2011.
- [20] C. Park, S. Lee, G.-H. Cho, S.-Y. Choi, and C. T. Rim, "Two-dimensional inductive power transfer system for mobile robots using evenly displaced multiple pickups," *IEEE Trans. Ind. Appl.*, vol. 50, no. 1, pp. 558–565, Jan. 2014.
- [21] J. Kim, D.-H. Kim, J. Choi, K.-H. Kim, and Y.-J. Park, "Free-positioning wireless charging system for small electronic devices using a bowl-shaped transmitting coil," *IEEE Trans. Microw. Theory Techn.*, vol. 63, no. 3, pp. 791–800, Mar. 2015.
- [22] M. J. Chabalko, M. Shahmohammadi, and A. P. Sample, "Quasistatic cavity resonance for ubiquitous wireless power transfer," *PLoS ONE*, vol. 12, no. 2, Feb. 2017, Art. no. e0169045.
- [23] T. Sasatani, C. J. Yang, M. J. Chabalko, Y. Kawahara, and A. P. Sample, "Room-wide wireless charging and load-modulation communication via quasistatic cavity resonance," *Proc. ACM Interact. Mob. Wearable Ubiquitous Technol.*, vol. 2, no. 4, pp. 188:1–188:23, Dec. 2018.
- [24] T. Sasatani, M. J. Chabalko, Y. Kawahara, and A. P. Sample, "Multimode quasistatic cavity resonators for wireless power transfer," *IEEE Antennas Wireless Propag. Lett.*, vol. 16, pp. 2746–2749, Aug. 2017.
- [25] K. Miwa, H. Mori, N. Kikuma, H. Hirayama, and K. Sakakibara, "A consideration of efficiency improvement of transmitting coil array in wireless power transfer with magnetically coupled resonance," in *Proc. IEEE Wireless Power Transf. (WPT)*, Perugia, Italy, May 2013, pp. 13–16.
- [26] B. Wang, W. Yerazunis, and K. H. Teo, "Wireless power transfer: Metamaterials and array of coupled resonators," *Proc. IEEE*, vol. 101, no. 6, pp. 1359–1368, Jun. 2013.
- [27] R. Takahashi, T. Sasatani, F. Okuya, Y. Narusue, and Y. Kawahara, "A cuttable wireless power transfer sheet," *Proc. ACM Interact. Mobile Wearable Ubiquitous Technol.*, vol. 2, no. 4, pp. 190:1–190:25, Dec. 2018.
- [28] K. Sumiya, T. Sasatani, Y. Nishizawa, K. Tsushio, Y. Narusue, and Y. Kawahara, "Alvus: A reconfigurable 2-d wireless charging system," *Proc. ACM Interact. Mobile Wearable Ubiquitous Technol.*, vol. 3, no. 2, pp. 68:1–68:29, Jun. 2019.
- [29] T. Arakawa, S. Goguri, J. V. Krogmeier, A. Kruger, D. J. Love, R. Mudumbai, and M. A. Swabey, "Optimizing wireless power transfer from multiple transmit coils," *IEEE Access*, vol. 6, pp. 23828–23838, Apr. 2018.
- [30] M. Su, Z. Liu, Q. Zhu, and A. P. Hu, "Study of maximum power delivery to movable device in omnidirectional wireless power transfer system," *IEEE Access*, vol. 6, pp. 76153–76164, Nov. 2018.
- [31] K. Mori, H. Lim, S. Iguchi, K. Ishida, M. Takamiya, and T. Sakurai, "Positioning-free resonant wireless power transmission sheet with staggered repeater coil array (SRCA)," *IEEE Antennas Wireless Propag. Lett.*, vol. 11, pp. 1710–1713, 2012.
- [32] S. M. Alamouti, "A simple transmit diversity technique for wireless communications," *IEEE J. Sel. Areas Commun.*, vol. 16, no. 8, pp. 1451–1458, Oct. 1998.
- [33] H. Abe, K. Irie, T. Tsujimoto, H. Gotoh, S. Sakamoto, and A. Yabuta, "Equivalent circuit applicable to free positioning wireless power transmission of apparatus having plural secondary coils (in Japanese)," *IEICE Tech. Rep.*, vol. 112, no. 282, pp. 25–30, Nov. 2012.
- [34] S. B. Lee and I. G. Jang, "Layout optimization of the secondary coils for wireless power transfer systems," in *Proc. IEEE Wireless Power Transf. Conf. (WPTC)*, Boulder, CO, USA, May 2015, pp. 1–4.

- [35] J. Kim, J. Kim, S. Kong, H. Kim, I.-S. Suh, N. P. Suh, D.-H. Cho, J. Kim, and S. Ahn, "Coil design and shielding methods for a magnetic resonant wireless power transfer system," *Proc. IEEE*, vol. 101, no. 6, pp. 1332–1342, Jun. 2013.
- [36] E. E. Altshuler, "Electrically small self-resonant wire antennas optimized using a genetic algorithm," *IEEE Trans. Antennas Propag.*, vol. 50, no. 3, pp. 297–300, Mar. 2002.
- [37] R. L. Haupt and D. H. Werner, *Genetic Algorithms in Electromagnetics*. Hoboken, NJ, USA: Wiley, 2007.
- [38] S. Song and R. D. Murch, "An efficient approach for optimizing frequency reconfigurable pixel antennas using genetic algorithms," *IEEE Trans. Antennas Propag.*, vol. 62, no. 2, pp. 609–620, Feb. 2014.
- [39] R. L. Haupt, "Antenna design with a mixed integer genetic algorithm," *IEEE Trans. Antennas Propag.*, vol. 55, no. 3, pp. 577–582, Mar. 2007.
- [40] J. Bito, S. Jeong, and M. M. Tentzeris, "A real-time electrically controlled active matching circuit utilizing genetic algorithms for wireless power transfer to biomedical implants," *IEEE Trans. Microw. Theory Techn.*, vol. 64, no. 2, pp. 365–374, Feb. 2016.
- [41] S. A. G. Shirazi and M. B. Menhaj, "A new genetic based algorithm for channel assignment problems," in *Computational Intelligence, Theory and Applications*. Jan. 2006, pp. 85–91.
- [42] T. Sasatani, Y. Narusue, Y. Kawahara, and T. Asami, "Genetic algorithm-based design of receiving resonator arrays for wireless power transfer via magnetic resonant coupling," in *Proc. IEEE Wireless Power Transf. Conf. (WPTC)*, Aveiro, Portugal, May 2016, pp. 1–4.
- [43] N. Y. Kim, K. Y. Kim, and C.-W. Kim, "Automated frequency tracking system for efficient mid-range magnetic resonance wireless power transfer," *Microw. Opt. Technol. Lett.*, vol. 54, no. 6, pp. 1423–1426, Jun. 2012.
- [44] R. Tseng, B. von Novak, S. Shevde, and K. A. Grajski, "Introduction to the alliance for wireless power loosely-coupled wireless power transfer system specification version 1.0," in *Proc. IEEE Wireless Power Transf. (WPT)*, Perugia, Italy, May 2013, pp. 79–83.
- [45] M. Zargham and P. G. Gulak, "Maximum achievable efficiency in near-field coupled power-transfer systems," *IEEE Trans. Biomed. Circuits Syst.*, vol. 6, no. 3, pp. 228–245, Jun. 2012.
- [46] Y. Narusue, Y. Kawahara, and T. Asami, "Maximizing the efficiency of wireless power transfer with a receiver-side switching voltage regulator," *Wireless Power Transf.*, vol. 4, no. 1, pp. 42–54, Feb. 2017.
- [47] I. Awai, "Basic characteristics of 'Magnetic resonance' wireless power transfer system excited by a 0 ohm power source," *IEICE Electron. Express*, vol. 10, no. 21, pp. 1–13, Nov. 2013.
- [48] P. Siarry, *Metaheuristics*. Cham, Switzerland: Springer, 2017.
- [49] X.-S. Yang, *Engineering Optimization: An Introduction with Metaheuristic Applications*. Hoboken, NJ, USA: Wiley, 2010.
- [50] MathWorks. *Global Optimization Toolbox*. Accessed: Oct. 17, 2019. [Online]. Available: <https://www.mathworks.com/help/gads/index.html>
- [51] K. K. Ean, B. T. Chuan, T. Imura, and Y. Hori, "Impedance matching and power division algorithm considering cross coupling for wireless power transfer via magnetic resonance," in *Proc. Intelec*, Sep. 2012, pp. 1–5.
- [52] T. Sasatani, Y. Narusue, and Y. Kawahara, "Dynamic complex impedance tuning method using a multiple-input DC/DC converter for wireless power transfer," in *Proc. IEEE Wireless Power Transf. Conf. (WPTC)*, Jun. 2018, pp. 1–4.
- [53] B. H. Choi, E. S. Lee, Y. H. Sohn, G. C. Jang, and C. T. Rim, "Six degrees of freedom mobile inductive power transfer by crossed dipole Tx and Rx coils," *IEEE Trans. Power Electron.*, vol. 31, no. 4, pp. 3252–3272, Apr. 2016.
- [54] N. S. Jeong and F. Carobolante, "Wireless charging of a metal-body device," *IEEE Trans. Microw. Theory Techn.*, vol. 65, no. 4, pp. 1077–1086, Apr. 2017.
- [55] M. Srinivas and L. M. Patnaik, "Genetic algorithms: A survey," *Computer*, vol. 27, no. 6, pp. 17–26, Jun. 1994.
- [56] T. Kawabe and T. Tagami, "A real coded genetic algorithm for matrix inequality design approach of robust PID controller with two degrees of freedom," in *Proc. 12th IEEE Int. Symp. Intell. Control*, Jul. 1997, pp. 119–124.



**TAKUYA SASATANI** (Graduate Student Member, IEEE) received the B.E. degree in electrical and electronic engineering and the M.S. degree in information science and technology from The University of Tokyo, Japan, in 2016 and 2018, respectively, where he is currently pursuing the Ph.D. degree with the Graduate School of Information Science and Technology. In 2017, he worked as a Lab Associate Researcher at Disney Research Pittsburgh. He is currently a Research Fellow with the Japan Society for the Promotion of Science (JSPS). His studies focus on empowering the Internet of Things through exploring novel approaches for ubiquitous wireless power transfer and low-power communication systems. He is a Student Member of ACM, IEICE, and IPSJ.



**YOSHIKI NARUSUE** (Member, IEEE) received the B.E., M.E., and Ph.D. degrees from the Graduate School of Information Science and Technology, The University of Tokyo, Tokyo, Japan, in 2012, 2014, and 2017, respectively. He is currently a Research Associate with the Department of Electrical Engineering and Information Systems, The University of Tokyo. His research interests include wireless power transfer, next-generation wireless communication systems, and the Internet of Things. He is a member of IEICE and IPSJ. He received the Second-Best Student Paper Award at IEEE RWS 2013, the Best Paper Award at IEEE CCNC 2018, and the ACM IMWUT Distinguished Paper Award in 2020.



**YOSHIHIRO KAWAHARA** (Member, IEEE) received the B.E., M.E., and Ph.D. degrees in information and communication engineering from The University of Tokyo, Tokyo, Japan, in 2000, 2002, and 2005, respectively. He joined the faculty in 2005. From 2011 to 2013, he was a Visiting Scholar with the Georgia Institute of Technology, Atlanta, GA, USA. He was a Visiting Assistant Professor with the Massachusetts Institute of Technology, Cambridge, MA, USA, in 2013. He is currently a Professor with the Department of Electrical Engineering and Information Systems, The University of Tokyo. His research interests include computer networks and ubiquitous and mobile computing. He is currently interested in developing energetically autonomous information communication devices. He is a member of ACM, IEICE, and IPSJ.

• • •